

Microwave assisted optical waveguide in Rydberg atoms

Nawaz Sarif Mallick^{1,*} and Tarak Nath Dey^{1,†}

¹*Department of Physics, Indian Institute of Technology Guwahati, Guwahati, Assam 781039, India*
(Dated: October 9, 2020)

We theoretically demonstrate an efficient scheme to build a micro-wave (MW) assisted optical waveguide in an inhomogeneously broadened vapor medium that is made of active ^{87}Rb atoms and inactive buffer gas atoms. We exploit the sensitive behaviour of MW field coupled between highly excited Rydberg states to create distinctly responsive and tunable atomic waveguide. The buffer gas induced collision further manipulates the features of the waveguide by widening the spatial transparency window and enhancing the contrast of the refractive index. We numerically solve Maxwell's equations to demonstrate diffractionless propagation of $5\ \mu\text{m}$ narrow paraxial light beams of arbitrary mode to several Rayleigh lengths. The presence of the buffer gas significantly enhances output intensity of the diffraction controlled light beam from 10% to 54%. This efficient diffraction elimination technique has important applications in high-resolution imaging and high-density optical communication.

PACS numbers: 42.65.Wi, 42.50.Gy, 78.70.Gq

I. INTRODUCTION

The ability to guide a narrow width optical beam holds promise for applications in high-density optical communication [1] and high-resolution imaging [2, 3]. The main obstacle for realisation of narrow beam based optical technology comes from diffraction and absorption of the medium [4]. The divergence angle of a narrow beam is significantly larger as compared to a broad beam due to its geometrical shape [5]. Consequently, the narrow beam encounters severe spatial distortions along the transverse direction as it propagates a few Rayleigh wavelengths distance through the medium. Ultimately diffraction induced image blurring prevents its use in the important light based applications [1, 2]. Hence, the complete elimination of diffraction for the narrow width beam becomes a long-standing goal.

To achieve this goal, different methods based on Raman self-focusing technique [6–8], and manipulation of refractive index [9–12] have been proposed for bulk media [8, 10] as well as for atomic vapor media [9, 12]. Suitable tailoring of refractive index along transverse direction leads to the formation of waveguide like structure inside cold atomic media [11, 13, 14] and also in hot vapor cells [9, 15, 16]. Truscott *et al.* published their seminal paper establishing that an atomic vapor can produce a waveguide which controls beam propagation without diffraction [15]. This experiment opened a floodgate for numerous experiments [15, 17–20] in addition to theoretical investigations [9, 12–14, 16, 17, 21, 22]. A suitably chosen spatial profile of the control field that creates spatial modulation of refractive index enables weak optical beams to propagate through the medium without loss of generality. Taking advantage of different spatial profiles of

control field such as Gaussian [13, 17, 23], super-Gaussian [13, 16] and different modes of Laguerre-Gaussian (LG_n^l) [12, 21, 24] results in an undistorted probe beam dynamics. Off-resonance [12, 16] or nearly resonance atomic transitions [21, 25] can also support guiding and steering of optical beams. However, the optically written waveguide is based on normal atoms with low principal quantum number and is often associated with considerable amount of absorption which limits lossless beam propagation to several Rayleigh lengths. Another drawback of normal atomic waveguide appears due to its lack of high contrast in refractive index between core and cladding that fails to support narrow beam propagation. These limitations can be overcome by exploiting the exaggerated optical properties of Rydberg atoms with high principal quantum number [26]. An atomic waveguide with narrow core and high contrast refractive index is a very fundamental criteria for guiding a narrow beam with size of the order of $5\ \mu\text{m}$.

In this article, we use highly excited Rydberg energy states of Rubidium atom to create high contrast and narrow core optical waveguide. The inspiration of our work comes from recent experimental demonstration of Shaffer *et al.* [27] in which MW field becomes highly responsive to the Rydberg energy states [27–30]. Even a very weak MW field ($8\ \mu\text{V cm}^{-1}$) is able to modify the probe response drastically [27]. We exploit this sensitive behavior of Rydberg energy states to create a highly efficient and extremely tunable atomic waveguide. A high contrast refractive index modulation of probe can be obtained by application of Bessel-Gaussian (BG) shaped MW beam which couples two highly excited Rydberg states $|30D_{\frac{5}{2}}\rangle$, $|31P_{\frac{3}{2}}\rangle$ [28]. The desired spatial shape of the beam either in MW or optical domain can be found experimentally [31–35]. Note that the strength of the dipole-dipole interactions mediated through the residual occupation in Rydberg states are very small in the considered model system [27, 28, 36, 37] and can be neglected safely.

Further, we assimilate inactive buffer gas atoms in ad-

* nawaz.phy@gmail.com

† tarak.dey@iitg.ac.in

dition to active Rydberg atoms inside the vapor cell to enhance the efficiency of the waveguide [18, 20, 38]. The active atoms frequently collide with the buffer gas atoms in which the velocity of the former alter from one velocity group to another velocity group. This velocity changing collision (VCC) leads to the phenomena of Dicke narrowing [39, 40] in presence of buffer gas. In this article, we exploit buffer gas induced VCC process in order to create a high contrast and efficient atomic waveguide. The perspective of the current scheme is substantially unique from the preceding articles in two ways [18, 20, 21]. First, the key difference is the use of spatially modulated MW beam between the Rydberg states. The spatial dependent MW BG beam generates a sharply varying fiber-like refractive index profile which is tightly confined in the central region of the waveguide. Second, the presence of buffer gas further manipulates the features of the waveguide by widening the transparency window and enhancing the contrast of the refractive index profile. Therefore, the transmission of the weak diffraction controlled probe beam at medium output enhances from 10% to 54% in the presence of buffer gas, unlike the results based on the absorptive systems reported earlier [18, 20, 21]. Also the enhanced contrast in refractive index focuses the probe beam tightly towards the center of the waveguide. Along with that the waveguide possesses an exclusive and handy feature. Its absorption and refractive index profile are squeezed from both sides with changing order of the BG beam, which makes this waveguide very efficient in guiding the probe beam of arbitrary width. A narrow beam broadens much faster than the wide beam because the divergence angle is inversely proportional to the beam width. Therefore, this high contrast and tunable atomic waveguide is essential for diffraction elimination from the narrow beam of any arbitrary mode.

The paper is structured as follows. In section II, we introduce the model configuration and describe the interaction of Rydberg atoms with the optical and MW fields by a semi-classical density matrix formalism. In section III, we point out the advantage of using a Rydberg atomic system over its normal counterpart by studying the probe susceptibility. In section IV, we display how the spatial structure of the MW beam permits us to build an optical waveguide. In section V, we discuss the tunability of the atomic waveguide. Section VI demonstrates the propagation of weak probe field having different beam profiles through the atomic waveguide. Finally, we briefly conclude our work in section VII.

II. THEORETICAL MODEL

A. Model Configuration

In this work, we study the collective behavior of active Rydberg atoms in the presence of inactive buffer gas atoms at room-temperature. The geometry of the model system under consideration is shown in Fig.

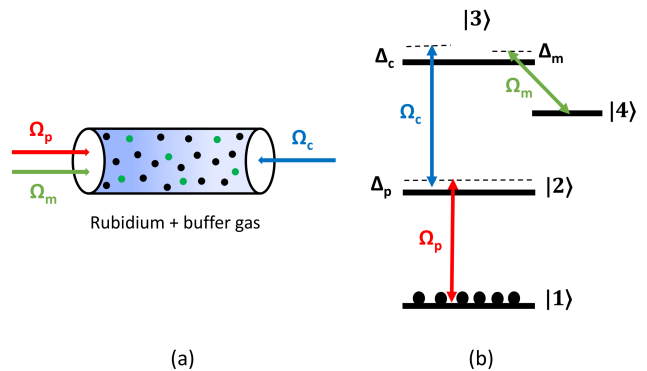


Figure 1. (a) A simple illustration of the model system. The vapor cell contains active Rubidium atoms (black dots) and inactive buffer gas atoms (green dots). Two counter-propagating optical fields Ω_p , Ω_c and one MW field interact with the active atoms. (b) Schematic representation of the four level system. The energy levels have been realized in ^{87}Rb atomic vapor where $|1\rangle=|5S_{\frac{1}{2}}, F=2, m_F=2\rangle$, $|2\rangle=|5P_{\frac{3}{2}}, F=3, m_F=3\rangle$, $|3\rangle=|30D_{\frac{5}{2}}, m_J=\frac{5}{2}\rangle$, $|4\rangle=|31P_{\frac{3}{2}}, m_J=\frac{3}{2}\rangle$.

1(a) where two counter propagating optical fields and MW field interact with the active ^{87}Rb atoms. Figure 1(b) shows four energy levels of active atoms which include one metastable ground state $|1\rangle$ and three excited states $|2\rangle$, $|3\rangle$, $|4\rangle$ [27, 28]. The ground state $|1\rangle=|5S_{\frac{1}{2}}, F=2, m_F=2\rangle$ is coupled to an excited state $|2\rangle=|5P_{\frac{3}{2}}, F=3, m_F=3\rangle$ by a weak probe field. Two highly excited Rydberg states $|3\rangle=|30D_{\frac{5}{2}}, m_J=\frac{5}{2}\rangle$ and $|4\rangle=|31P_{\frac{3}{2}}, m_J=\frac{3}{2}\rangle$ are coupled by a moderately intense MW field of frequency 84.2 GHz [28]. A strong control field connects two states $|2\rangle$ and $|3\rangle$. The electric fields associated with the electro-magnetic (EM) radiations are described as

$$\vec{E}_j(\vec{r}, t) = \hat{e}_j \mathcal{E}_j(\vec{r}) e^{i(k_j z - \omega_j t)} + c.c., \quad (1)$$

where $\mathcal{E}_j(\vec{r})$, k_j , ω_j and \hat{e}_j are the slowly varying envelope, wave number, frequency and unit polarization vector of the EM fields respectively. The indices $j \in \{p, c, m\}$ refer to the probe, control and MW field. The EM fields only interact with the active atoms and the interaction can be expressed as a time-dependent Hamiltonian under the electric dipole approximation :

$$\begin{aligned} H' = & \hbar\omega_{21} |2\rangle \langle 2| + \hbar(\omega_{21} + \omega_{32}) |3\rangle \langle 3| \\ & + \hbar(\omega_{21} + \omega_{32} - \omega_{34}) |4\rangle \langle 4| - \hbar\Omega_p e^{-i\omega_p t} |2\rangle \langle 1| \\ & - \hbar\Omega_c e^{-i\omega_c t} |3\rangle \langle 2| - \hbar\Omega_m e^{-i\omega_m t} |3\rangle \langle 4| + h.c., \end{aligned} \quad (2)$$

where Ω_p , Ω_c , Ω_m are the Rabi frequencies of the probe, control and MW fields respectively. The expression of

Rabi frequencies are

$$\Omega_p = \frac{\vec{d}_{21} \cdot \hat{e}_p}{\hbar} \mathcal{E}_p, \quad \Omega_c = \frac{\vec{d}_{32} \cdot \hat{e}_c}{\hbar} \mathcal{E}_c \quad \text{and} \quad \Omega_m = \frac{\vec{d}_{34} \cdot \hat{e}_m}{\hbar} \mathcal{E}_m. \quad (3)$$

In order to acquire the time-independent Hamiltonian, we execute the following unitary transformation

$$H = U^\dagger H' U - i\hbar U^\dagger \frac{\partial U}{\partial t}, \quad (4)$$

where U is defined as

$$U = e^{-i(\omega_p|2\rangle\langle 2| + (\omega_p + \omega_c)|3\rangle\langle 3| + (\omega_p + \omega_c - \omega_m)|4\rangle\langle 4|)t}. \quad (5)$$

Now the Hamiltonian transforms into the following time-independent form

$$\begin{aligned} H = & -\hbar\Delta_p |2\rangle\langle 2| - \hbar(\Delta_p + \Delta_c) |3\rangle\langle 3| \\ & - \hbar(\Delta_p + \Delta_c - \Delta_m) |4\rangle\langle 4| - \hbar\Omega_p |2\rangle\langle 1| \\ & - \hbar\Omega_c |3\rangle\langle 2| - \hbar\Omega_m |3\rangle\langle 4| + h.c. \end{aligned} \quad (6)$$

where $\Delta_p = \omega_p - \omega_{21}$, $\Delta_c = \omega_c - \omega_{32}$, and $\Delta_m = \omega_m - \omega_{34}$, are the detuning of the probe, control and MW fields respectively. The resonant transition frequency between energy levels $|1\rangle \leftrightarrow |2\rangle$, $|2\rangle \leftrightarrow |3\rangle$ and $|3\rangle \leftrightarrow |4\rangle$ are denoted by ω_{21} , ω_{32} and ω_{34} , respectively.

B. Dynamical Equations

The dynamics of the active atoms inside the vapor cell are governed by the following Liouville's equation :

$$\dot{\rho} = -\frac{i}{\hbar}[H, \rho] + \mathcal{L}_\rho \quad (7)$$

where the second term incorporates various radiative and non-radiative decay processes in the presence of buffer gas atoms. The collisions between the active atoms and buffer gas atoms change the velocity distribution of the active atoms inside the medium. These collisions also affect the phase coherence between the atomic energy levels which modifies the life-time of the atomic coherence [41–45]. The effect of such collisions can be included in the dynamical Eq. (7) by adding the following term [41, 42, 44]

$$\begin{aligned} \left[\frac{\partial \rho_{jk}(v, t)}{\partial t} \right]_{\text{collision}} = & -\gamma_{ph}(1 - \delta_{jk})\rho_{jk}(v, t) \\ & - \Gamma_{jk}\rho_{jk}(v, t) + \int K(v' \rightarrow v)\rho_{jk}(v', t)dv' \end{aligned} \quad (8)$$

In the above Eq. (8), Γ_{jk} is known as velocity changing collision rate and γ_{ph} is the rate of collisional dephasing of the atomic coherence. The collision kernel, $K(v' \rightarrow v)$ represents the probability density per unit time that active atoms have when their velocity change from v' to v as a result of collisions with buffer gas atoms [41]. For

simplicity, the collision kernel can be written in terms of Γ_{jk} as shown in the following expression

$$\begin{aligned} K(v' \rightarrow v) = & \Gamma_{jk}M(v), \\ M(v) = & \frac{1}{\sqrt{\pi}v_{th}} e^{-\frac{v^2}{v_{th}^2}}, \quad v_{th} = \sqrt{\frac{2k_B T}{m_A}}, \end{aligned} \quad (9)$$

where $M(v)$ and v_{th} are the Maxwell-Boltzmann velocity distribution along the z direction and most probable velocity of the active atoms of mass m_A at a temperature T . The spontaneous decay rates from the excited state $|j\rangle$, ($j \in 2, 3, 4$) to the ground state $|1\rangle$, are denoted by γ_{j1} . Note that the collision rates of different atomic states Γ_{j1} , $j \in 2, 3, 4$ are all similar in strength and are indicated by $\Gamma_{21} \simeq \Gamma_{31} \simeq \Gamma_{41} = \Gamma_c$ [44]. In the considered model system, k_p ($\simeq 2\pi \times 1.3 \mu\text{m}^{-1}$) is nearly equal to k_c ($\simeq 2\pi \times 2.0 \mu\text{m}^{-1}$) such that the wave vector difference $|\delta\vec{k}| = |\vec{k}_p - \vec{k}_c|$ becomes minimal. Further, we restrict our analysis for the moderate collision case in which Γ_c is comparatively smaller than spontaneous decay rate (γ_{21}) and Doppler width (γ_d) *i.e.* $\Gamma_c \ll \gamma_{21}, \gamma_d$ [27, 44]. The degree of collisions can be realized experimentally by controlling the density of the buffer gas inside the vapor cell. The collision induced Γ_c significantly influences the absorptive and dispersive features of the atomic medium.

The following three coupled density matrix equations are sufficient for describing the dynamics of the active atoms in the buffer gas environment under weak probe approximation

$$\begin{aligned} \dot{\rho}_{21}(v, t) = & -A_{21}(v)\rho_{21}(v, t) + i\Omega_p(\rho_{11}(v, t) - \rho_{22}(v, t)) \\ & + i\Omega_c^*\rho_{31}(v, t), \\ \dot{\rho}_{31}(v, t) = & -A_{31}(v)\rho_{31}(v, t) + i\Omega_c\rho_{21}(v, t) - i\Omega_p\rho_{32}(v, t) \\ & + i\Omega_m\rho_{41}(v, t) + \Gamma_{31}M(v) \int \rho_{31}(v, t)dv, \\ \dot{\rho}_{41}(v, t) = & -A_{41}(v)\rho_{41}(v, t) + i\Omega_m^*\rho_{31}(v, t) - i\Omega_p\rho_{42}(v, t) \\ & + \Gamma_{41}M(v) \int \rho_{41}(v, t)dv, \end{aligned}$$

where

$$\begin{aligned} A_{21}(v) = & i(\vec{k}_p \cdot \vec{v} - \Delta_p) + \gamma_{21} + \Gamma_{21} + \gamma_{ph}, \\ A_{31}(v) = & i\{(\vec{k}_p + \vec{k}_c) \cdot \vec{v} - (\Delta_p + \Delta_c)\} + \gamma_{31} + \Gamma_{31} + \gamma_{ph}, \\ A_{41}(v) = & i\{(\vec{k}_p + \vec{k}_c - \vec{k}_m) \cdot \vec{v} - (\Delta_p + \Delta_c - \Delta_m)\} \\ & + \gamma_{41} + \Gamma_{41} + \gamma_{ph}. \end{aligned}$$

The perturbative solution of the atomic coherence and population in the limits of weak probe approximation can be defined as

$$\rho_{jk} = \rho_{jk}^{(0)} + \Omega_p \rho_{jk}^{(1)}. \quad (10)$$

The zeroth order solution in the absence of probe field is $\rho_{11}^{(0)} = M(v)$ [44]. The first order solutions in the presence

of weak probe field can be obtained in the following forms

$$\begin{aligned}\dot{\rho}_{21}^{(1)}(v, t) &= -A_{21}(v)\rho_{21}^{(1)}(v, t) + i\rho_{11}^{(0)} + i\Omega_c^*\rho_{31}^{(1)}(v, t), \\ \dot{\rho}_{31}^{(1)}(v, t) &= -A_{31}(v)\rho_{31}^{(1)}(v, t) + i\Omega_c\rho_{21}^{(1)}(v, t) \\ &\quad + i\Omega_m\rho_{41}^{(1)}(v, t) + \Gamma_{31}M(v) \int \rho_{31}^{(1)}(v, t)dv, \\ \dot{\rho}_{41}^{(1)}(v, t) &= -A_{41}(v)\rho_{41}^{(1)}(v, t) + i\Omega_m^*\rho_{31}^{(1)}(v, t) \\ &\quad + \Gamma_{41}M(v) \int \rho_{41}^{(1)}(v, t)dv.\end{aligned}$$

The steady state response of the above coupled equations *i.e.*, $\dot{\rho}_{jk}^{(1)} = 0$ can be used for finding the analytical expression of first order atomic coherences $\langle\rho_{21}\rangle$, $\langle\rho_{31}\rangle$ and $\langle\rho_{41}\rangle$. We also incorporated the thermal agitation of the atom by performing the velocity averaging of the atomic coherence

$$\begin{aligned}\langle\rho_{21}\rangle &= \int \rho_{21}^{(1)}(v)dv, \\ &= i\Omega_P f_{10} + i\Omega_c^*\Gamma_{31}f_3\langle\rho_{31}^{(1)}\rangle \\ &\quad - \Omega_c^*\Omega_m\Gamma_{41}f_1\langle\rho_{41}^{(1)}\rangle, \\ \langle\rho_{31}^{(1)}\rangle &= \int \rho_{31}^{(1)}(v)dv, \\ &= \Omega_p\Omega_c \left[\frac{|\Omega_m|^2 f_1 L_2 - f_3 L_3}{L_1 L_3 + |\Omega_m|^2 L_2 L_4} \right], \\ \langle\rho_{41}^{(1)}\rangle &= \int \rho_{41}^{(1)}(v)dv, \\ &= -i\Omega_p\Omega_c\Omega_m^* \left[\frac{f_1 L_1 + f_3 L_4}{L_1 L_3 + |\Omega_m|^2 L_2 L_4} \right],\end{aligned}$$

where

$$\begin{aligned}L_1 &= 1 + |\Omega_c|^2\Gamma_{31}f_8 - \Gamma_{31}f_5, \\ L_2 &= \Gamma_{41}f_4 - |\Omega_c|^2\Gamma_{41}f_6, \\ L_3 &= 1 - |\Omega_c|^2|\Omega_m|^2\Gamma_{41}f_9 \\ &\quad - \Gamma_{41}f_2 + |\Omega_m|^2\Gamma_{41}f_7, \\ L_4 &= \Gamma_{31}f_4 - |\Omega_c|^2\Gamma_{31}f_6.\end{aligned}$$

The expression of the spatial functions f_j , ($j \in 1, 2, 3, \dots, 10$) are shown in the appendix section (15). Finally, the velocity averaged linear probe susceptibility, $\langle\chi_{21}\rangle$ at frequency ω_p can be written as

$$\langle\chi_{21}\rangle = \frac{\mathcal{N}|\vec{d}_{21}|^2}{\hbar\Omega_p}\langle\rho_{21}\rangle \quad (11)$$

where \mathcal{N} is the atomic density.

III. MICROWAVE FIELD SENSITIVITY

In this section, we distinguish the advantage of using Rydberg atomic system over its normal counterpart

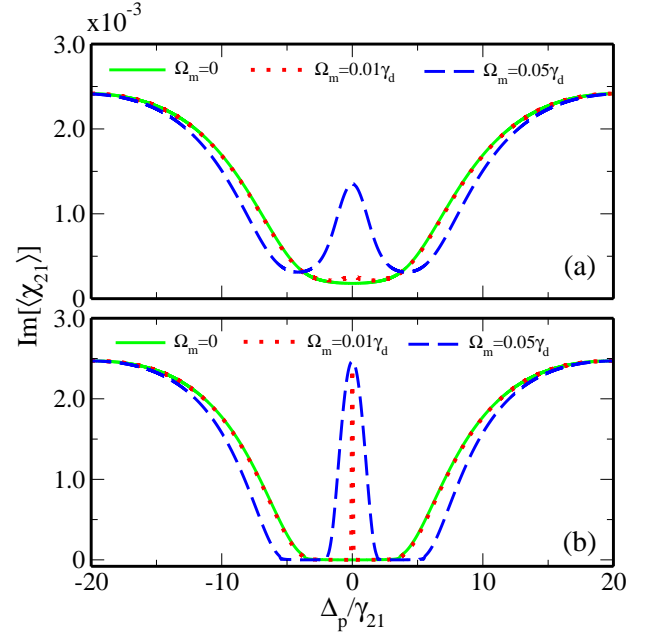


Figure 2. Probe absorption profile, $\text{Im}[\langle\chi_{21}\rangle]$ as a function of probe laser detuning (Δ_p) for (a) normal (b) Rydberg atomic system. EIA lineshapes for three different values of MW field (Ω_m) demonstrate the MW field sensitivity. Decay rate for (a) $\gamma_{31} \simeq \gamma_{41} \simeq \gamma_{21}$ and for (b) $\gamma_{31} = 2\pi \times 1.0 \times 10^3$ Hz, $\gamma_{41} = 2\pi \times 0.5 \times 10^3$ Hz. The other parameters are $\Omega_c = 0.3\gamma_d$, $\Delta_c = 0$, $\Delta_m = 0$, $\Gamma_c = 0$, $T=300\text{K}$, $\mathcal{N} = 5 \times 10^{10}$ atoms/cm³, $\gamma_d = 2.53 \times 10^9$ Hz, $\gamma_{21} = 2\pi \times 6.1 \times 10^6$ Hz, $\gamma_{ph} \approx 1 \times 10^3$ Hz.

by studying the probe susceptibility in the absence and presence of the MW field. The normal counterpart here refers to a low quantum number atomic system with $|3\rangle=|5D_{5/2}, m_J = 5/2\rangle$, $|4\rangle=|6P_{3/2}, m_J = 3/2\rangle$. In Rydberg atomic system, MW field couples two Rydberg states with high principal quantum number as shown in Fig. 1(b). Whereas MW field connects two states with very low principal quantum number for normal atomic system. In Fig. 2(a) and 2(b), we compare the probe absorption lineshape in case of normal as well as Rydberg atomic system for three different values of MW field intensity $\Omega_m=0, 0.01\gamma_d, 0.05\gamma_d$. In absence of MW field ($\Omega_m=0$), both the normal and Rydberg atomic systems display electromagnetically induced transparency (EIT) [46, 47] under two-photon resonance condition *i.e.*, $\Delta_p = \Delta_c$ as shown by solid green curves in Fig. 2. We have observed that the Rydberg system offers complete flat transparency window (no absorption) due to the low decay rate (\sim KHz) of the Rydberg states as compared to a shallow window in the normal atomic states (decay rate \sim MHz) [48]. We next study how a weak MW field ($\Omega_m=0.01\gamma_d$) drastically modifies the probe response in Rydberg systems which is distinct from a normal system. It is clear from 2(b) that a complete sharp electromagnetically induced absorption (EIA) peak [49, 50] is present in the Rydberg system. On the other hand, the EIA

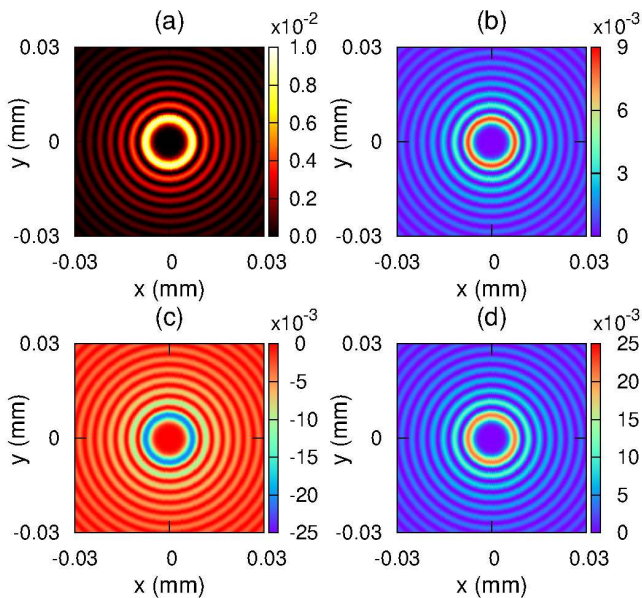


Figure 3. (a) Input ring-shaped Bessel-Gaussian (BG) MW beam, (b) Fiber-like absorption profile tightly confined in the central region of transverse position (x,y) with $\Delta_p = \pm 0.001\gamma_{21}$, (c) Blue shifted detuning ($\Delta_p = 0.001\gamma_{21}$) and (d) Red shifted detuning ($\Delta_p = -0.001\gamma_{21}$) depict waveguide like and anti-waveguide like refractive index profile in the transverse position (x,y) respectively. The parameters are $\Omega_c = 0.3\gamma_d$, $\Omega_m = 0.05\gamma_d$, $\omega_c = 60\mu m$, $\omega_m = 60\mu m$, $n = 7$. All other parameters are same as in 2.

peak in a normal atomic system just builds up as shown by the dotted red curve in Fig. 2(a). With the increase of MW field power ($\Omega_m=0.05\gamma_d$), Rydberg EIA peak experiences power broadening, while the normal EIA peak is still growing towards its maximum value. These observations clearly confirm that Rydberg energy states are strongly responsive to the MW field unlike the normal atomic states [27]. We exploit this responsive behavior of MW field in Rydberg atomic systems to create a highly tuneable atomic waveguide. The effective modulation of spatial susceptibility due to spatial structure of the MW beam holds the main essence behind the formation of waveguide inside the Rydberg atomic system.

IV. FORMATION OF ATOMIC WAVEGUIDE

We now investigate how the spatial structure of the MW beam permits us to build an optical waveguide inside the atomic medium. A waveguide like refractive index can be formed by considering the transverse profile of the MW beam to be Bessel-Gaussian (BG) together with a Gaussian (HG_0^0) shaped control beam. The spatial shape of the MW BG beam in cylindrical coordinate

can be expressed as [5],

$$\Omega_m(r, \phi, z = 0) = \Omega_m^0 \mathcal{J}_n(ar) e^{in\phi} e^{-\frac{r^2}{w_m^2}}; \quad (12)$$

$$r = \sqrt{x^2 + y^2}, \quad \phi = \tan^{-1}\left(\frac{y}{x}\right).$$

The input amplitude of BG beam is denoted by Ω_m^0 . The n th-order Bessel function of first kind is defined as $\mathcal{J}_n(ar)$, where a is a scale factor. The minimum beam waist of Gaussian part is w_m . The input spatial inhomogeneous intensity distribution of BG beam of order 7 is shown in Fig. 3(a). It is clear from Fig. 3(a) that the MW BG beam consists of many concentric rings which has zero intensity at the central region whereas maximum intensity occurs in the ring-shaped regions. Therefore, the MW BG beam together with Gaussian control beam can be used to obtain the desired spatial refractive profile of the probe beam as evident from the following discussion. Fig. 3(b) shows the transverse variation of the probe absorption. A complete transparency window exists at the core because of dominant characteristics of control beam over the MW field. The diminishing intensity of the control beam towards the wing region yields absorption at the cladding. Simultaneously, the MW field gains maximum intensity in the bright ring which causes high probe absorption due to EIA as shown in Fig. 3(b). Hence, considering a suitable spatial structure of the two fields, allows us to achieve probe transparency at the core and opaqueness at cladding, at both resonance condition as well as near resonance situation. Fig. 3(c) displays that the refractive index attains a maximum value at EIT dominant region and forms the core of the atomic waveguide. The cladding section of the waveguide can be cast by EIA, since EIT is ineffective in the ring-shaped region. The induced waveguide structure consists of refractive variation between core and cladding accompanied with a small width of the core. Hence the spatial response of the medium for the probe field exhibits waveguide like structure at blue detuned condition whereas at red detuned condition, it changes to the anti-waveguide like structure as shown in Fig. 3(d). In both the cases, the core region of the atomic wave guide display minimum absorption as shown in Fig. 3(b). Finally, we have chosen the blue detuned probe field condition, *i.e.*, $\Delta_p = 0.001\gamma_{21}$ for efficient guiding of various narrow Gaussian and Hermit Gaussian beams with arbitrary modes.

V. TUNABILITY OF THE WAVEGUIDE

Next, we discuss how the buffer gas induced collision significantly manoeuvres the features of the atomic waveguide along the transverse direction in the presence of MW field (Ω_m^0). In order to comprehend the reasons behind these manipulations of atomic waveguide, we plot the probe absorption lineshape as a function of Δ_p in the absence and presence of VCC as shown in Fig. 4(a). The MW induced EIA peak in Fig. 4(a) can be enhanced by a

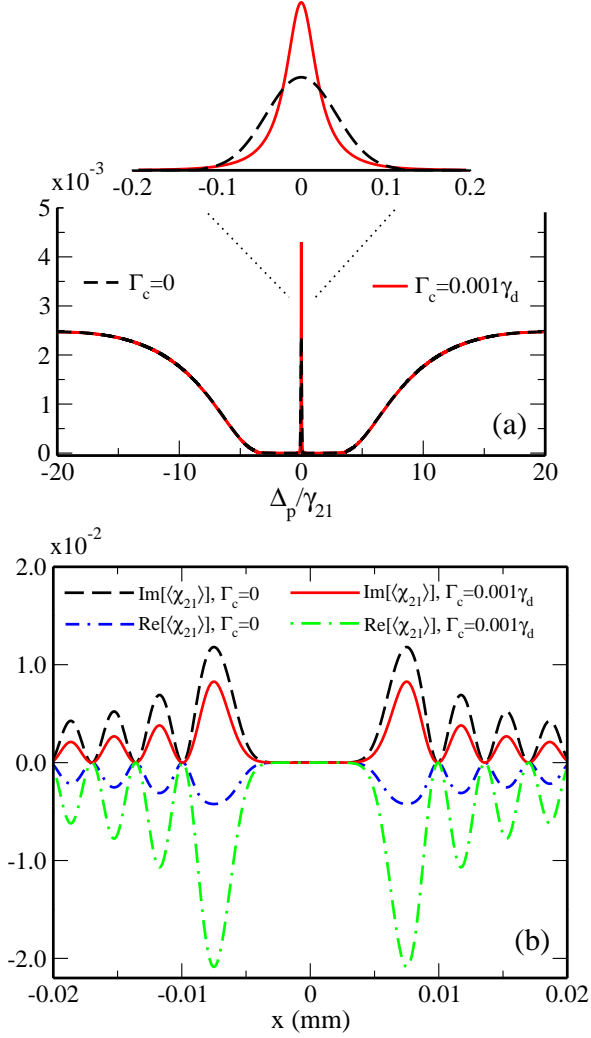


Figure 4. (a) Probe absorption is plotted as a function of probe field detuning in the presence and absence of VCC. Inset zoom figure shows the Dicke narrowing and enhancing of the EIA peak due to Γ_c . (b) Real and imaginary part of the susceptibility is plotted as a function of transverse position x at $y = 0$ plane for two different values of Γ_c . All other parameters are same as in 2.

notable amount in the presence of VCC. Along with that the EIA lineshape manifests Dicke like narrowing due to the collision process as displayed in the inset of Fig. 4(a). Fig. 4(b) illustrates that the contrast of refractive index significantly enhances in the presence of VCC. The slope of VCC induced refractive index profile is remarkably sharp which makes this waveguide more efficient in guiding the narrow probe beam in comparison to that of a Kerr field induced waveguide [21]. Further, the transparency window of the waveguide becomes much wider in the presence of the buffer gas. As a result, a narrow probe beam propagates through the waveguide without significant loss of intensity. These VCC induced Dicke

narrowing and enhancing of the EIA peak distinctly facilitates the waveguide characteristics.

Now, we delineate how the MW field intensity and BG beam order effect the induced atomic waveguide. In Fig. 5(a), we plot imaginary and real part of the probe susceptibility along the transverse position for two different values of MW field intensity. We observe that the difference of refractive index between the core and cladding of the waveguide is enhanced significantly with the increase of MW intensity. Fig. 5(b), depicts the variation of absorption and refractive index profile with the order of BG beam. A lower order BG beam squeezes the absorption profile and refractive index of the waveguide from both sides. These unique features create sharply varying and confined refractive index profiles which makes the waveguide very efficient in guiding the light beam. It is familiar that a narrow beam broadens more rapidly than a wide beam due to optical diffraction because divergence angle ($\Theta = 2\lambda_p/\pi w_p$) is inversely proportional

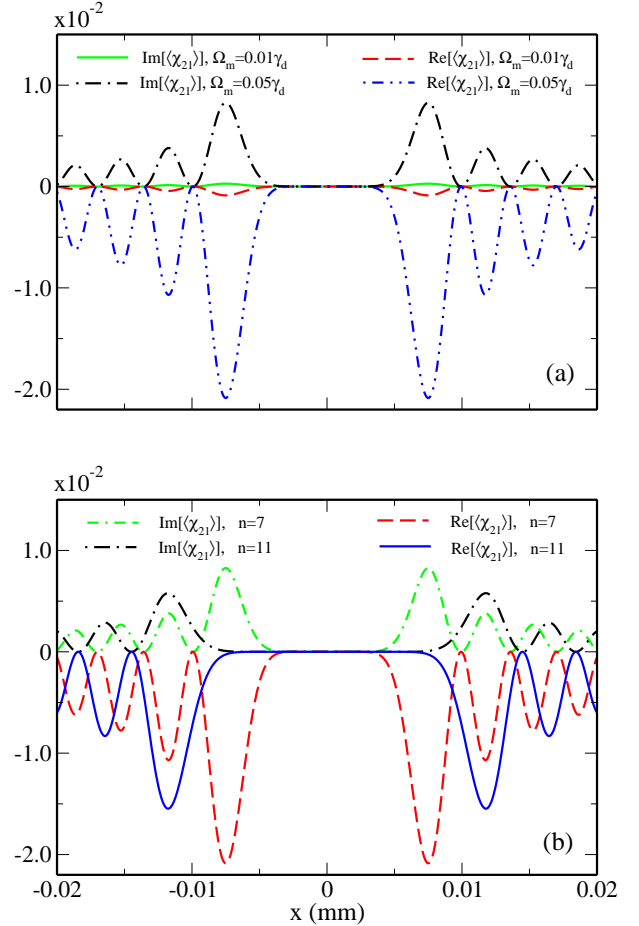


Figure 5. Medium susceptibility along the transverse position x at $y = 0$ plane is plotted for two different values of (a) MW field intensity and (b) BG beam order. The parameters are $\Omega_c = 0.3\gamma_d$, $\Delta_p = 0.001\gamma_{21}$, $\Gamma_c = 0.001\gamma_d$. All other parameters are same as in 2.

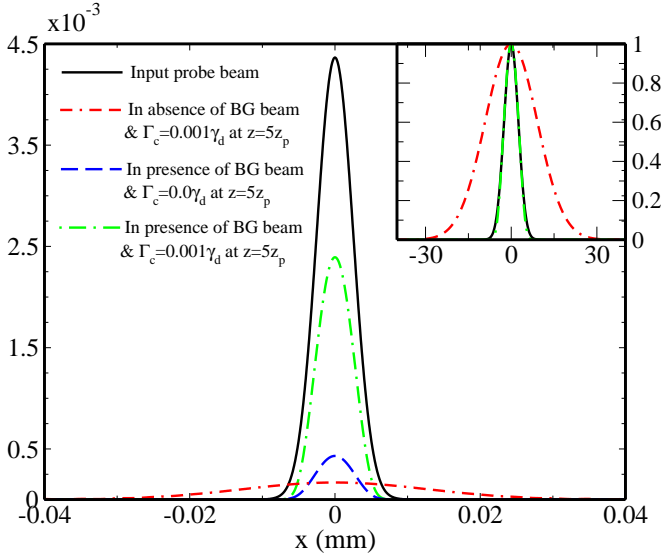


Figure 6. Narrow Gaussian beam ($\omega_p = 5\mu\text{m}$) propagation through the atomic medium in presence and absence of MW BG beam and buffer gas. Inset figure shows the normalised intensity profile of the probe beam in presence and absence of MW BG beam. All other parameters are same as in figure 5.

to the beam width w_p [5]. Hence, this high-contrast and squeezed waveguide is highly desired in order to remove diffraction from the narrow beam.

VI. BEAM PROPAGATION THROUGH THE WAVEGUIDE

Next, we study the propagation of weak probe field having different beam profiles through the atomic waveguide. The beam propagation dynamics is governed by the Maxwell's wave equations [12, 21]. Under slowly varying envelope and paraxial wave approximation, Maxwell's wave equations for the probe beam transform into the following form

$$\frac{\partial \Omega_p}{\partial z} = \frac{i}{2k_p} \nabla_{\perp}^2 \Omega_p + 2i\pi k_p \langle \chi_{21} \rangle \Omega_p. \quad (13)$$

In Eq. (13), second order partial derivative in the xy plane *i.e.* $\nabla_{\perp}^2 = (\partial^2/\partial x^2 + \partial^2/\partial y^2)$ incorporates inherent optical diffraction of the probe beam. The last term of Eq. (13) is the contribution of linear and nonlinear optical effects which includes MW and buffer gas induced absorption and refractive index profile of the medium in order to suppress the diffraction. Note that we have considered MW Bessel-Gaussian (BG) beam which can propagate through the atomic medium without diffraction. Also, the Rayleigh length of control beam is much larger than the length of the atomic medium. Therefore, we can safely neglect the diffraction of the control beam.

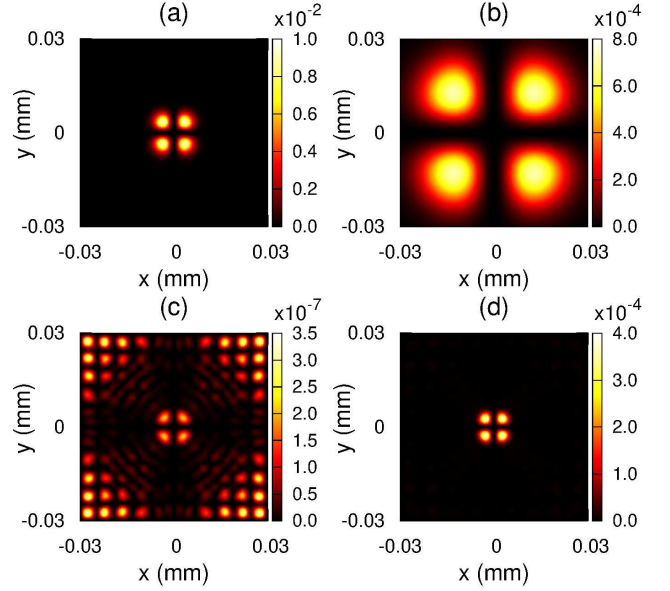


Figure 7. (a) Intensity profile of the probe beam (HG_1^1) at $z=0$. (b) Intensity profile of the probe beam (HG_1^1) in absence of MW BG beam at $z = 5z_p$. Intensity profile of the probe beam (HG_1^1) in presence of MW BG beam after propagation over 5 Rayleigh lengths ($z=5z_p$) through the atomic medium (c) without and (d) with the buffer gas environment. All other parameters are same as in figure 6.

We adopt split-step Fourier method (SSFM) to obtain the numerical solution of Eq. (13) and demonstrate the effect of spatially varying absorption and refractive index on probe beam dynamics. First, we study the propagation dynamics of a Gaussian (HG_0^0) probe beam. The width of the probe beam is $5\mu\text{m}$ which remains within the limit of paraxial wave approximation, $\lambda_p/2\pi w_p < 0.1$ [21, 51]. The propagation dynamics of the narrow Gaussian shaped probe beam through the high contrast atomic waveguide is shown in Fig. 6. The input and output intensity profile of the probe beam in the presence and absence of the MW beam and buffer gas are illustrated clearly. In absence of MW BG beam, the probe beam suffers diffraction induced broadening along with large absorption as shown with double-dashed-dot red curve in Fig. 6. The diffraction of the probe beam is drastically reduced in the presence of MW BG beam. We notice that the output intensity of the probe beam decreases below 10% in absence of buffer gas after the propagation of $z = 5z_p$. The situation changes in the presence of buffer gas, and the transmissivity of the diffraction controlled probe beam enhances over 54% for the same propagation distance ($z = 5z_p$). This efficient beam propagation without any diffraction is possible due to the presence of high-contrast tunable optical waveguide in buffer gas medium.

In order to prove the robustness of the atomic waveguide, we also demonstrate diffraction-less propagation of

arbitrary Hermite-Gaussian (HG_u^v) modes. A further reason to choose HG_u^v modes of narrow width is its direct application in super-resolution imaging [3, 52]. The spatial profile of different HG_u^v modes at its point of entering the medium ($z = 0$) is given by

$$\Omega_p(x, y, 0) = \Omega_p^0 H_u \left(\frac{\sqrt{2}x}{w_p} \right) H_v \left(\frac{\sqrt{2}y}{w_p} \right) e^{-\frac{x^2+y^2}{w_p^2}}, \quad (14)$$

where H_u and H_v are the Hermite polynomials of order u and v respectively. For demonstration, we propel the Hermite-Gaussian probe beam of mode $u = 1$, $v = 1$ through the waveguide. The intensity profile of the HG₁¹ mode at $z = 0$ is shown in Fig. 7(a). The diffraction of the beam in absence of MW BG beam and buffer gas is displayed in Fig. 7(b). The presence of BG beam and buffer gas eliminates the diffraction completely as clearly shown in Fig. 7(d). However, Fig. 7(c) shows that in the absence of buffer gas medium, the waveguide fails to guide HG₁¹ beam due to the lack of sharply varying high contrast refractive index profile. The transverse structure of the MW beam and buffer gas play the important role in guiding the weak probe beam of narrow width and arbitrary modes.

VII. CONCLUSION

In conclusion, we have demonstrated an efficient scheme to generate MW assisted optical waveguide in an inhomogeneously broadened vapor medium that is made of active ⁸⁷Rb atoms and inactive buffer gas atoms. The sensitive behaviour of a MW field coupled between two highly excited Rydberg states of Rb atoms allow us to create a responsive atomic susceptibility. The structured MW BG beam and Gaussian control beam together build an optical waveguide with amenable fiber like refractive index profile. The presence of buffer gas induced collision further manipulates the features of the waveguide by widening the spatial transparency window and enhancing the contrast of the refractive index. Changing the order of the MW BG beam squeezes the high contrast waveguide from both sides, which can successfully guide the probe beam of narrow width. We numerically solve Maxwell's equations to

demonstrate diffractionless propagation of narrow paraxial light beams of arbitrary modes such as Gaussian, Hermite-Gaussian HG₁¹ to several Rayleigh lengths. The output intensity of the diffractionless light significantly enhances in the presence of a buffer gas. This efficient technique to eliminate diffraction from narrow light beams have important applications in high-density optical communication [1] and high-resolution imaging [2, 3, 52].

APPENDIX

$$\begin{aligned} f_1 &= \int \frac{M(v)}{f_D(v)} dv, & f_2 &= \int \frac{M(v)}{A_{41}(v)} dv, \\ f_3 &= \int \frac{A_{41}(v)M(v)}{f_D(v)} dv, \\ f_4 &= \int \frac{M(v)}{A_{31}(v)A_{41}(v) + |\Omega_m|^2} dv, \\ f_5 &= \int \frac{A_{41}(v)M(v)}{A_{31}(v)A_{41}(v) + |\Omega_m|^2} dv, \\ f_6 &= \int \frac{A_{41}(v)M(v)}{(A_{31}(v)A_{41}(v) + |\Omega_m|^2) f_D(v)} dv, \\ f_7 &= \int \frac{M(v)}{(A_{31}(v)A_{41}(v) + |\Omega_m|^2) A_{41}(v)} dv, \\ f_8 &= \int \frac{A_{41}^2(v)M(v)}{(A_{31}(v)A_{41}(v) + |\Omega_m|^2) f_D(v)} dv, \\ f_9 &= \int \frac{M(v)}{(A_{31}(v)A_{41}(v) + |\Omega_m|^2) f_D(v)} dv, \\ f_{10} &= \int \frac{M(v) (A_{31}(v)A_{41}(v) + |\Omega_m|^2)}{f_D(v)} dv, \end{aligned}$$

where

$$f_D(v) = A_{21}(v) (A_{31}(v)A_{41}(v) + |\Omega_m|^2) + A_{41}(v)|\Omega_c|^2.$$

ACKNOWLEDGMENT

T.N.D. and N.S.M. gratefully acknowledge funding by the Science and Engineering Research Board (Grant No. CRG/2018/000054). N.S.M thanks Prof Wenhui Li for useful discussions.

-
- [1] E. N. Glezer, M. Milosavljevic, L. Huang, R. J. Finlay, T.-H. Her, J. P. Callan, and E. Mazur, *Opt. Lett.* **21**, 2023 (1996).
[2] S. Feng and J. M. Elson, *Opt. Express* **14**, 216 (2006).
[3] M. Tsang, R. Nair, and X.-M. Lu, *Phys. Rev. X* **6**, 031033 (2016).
[4] R. Malallah, H. Li, I. Muniraj, D. Cassidy, N. Al-Attar, J. J. Healy, and J. T. Sheridan,

- J. Opt. Soc. Am. B* **35**, 2046 (2018).
[5] P. W. Milonni and J. H. Eberly, *Laser Physics* (John Wiley and Sons Inc, 2010).
[6] F. Ladouceur, D. J. Mitchell, and A. W. Snyder, *J. Opt. Soc. Am. B* **14**, 1768 (1997).
[7] L. Stoyanov, G. Maleshkov, I. Stefanov, and A. Dreischuh, *J. Opt. Soc. Am. B* **31**, 1159 (2014).

- [8] R. D. L. Fuente, A. Barthelemy, and C. Froehly, *Opt. Lett.* **16**, 793 (1991).
- [9] R. Kapoor and G. S. Agarwal, *Phys. Rev. A* **61**, 053818 (2000).
- [10] S.-L. Xu, M. R. Belić, D.-P. Cai, L. Xue, J.-R. He, and J. Cheng, *J. Opt. Soc. Am. B* **35**, 410 (2018).
- [11] T. G. Akin, S. P. Krzyzewski, M. W. Holtfrerich, and E. R. I. Abraham, *J. Opt. Soc. Am. B* **34**, 1286 (2017).
- [12] T. N. Dey and J. Evers, *Phys. Rev. A* **84**, 043842 (2011).
- [13] T. N. Dey and G. S. Agarwal, *Opt. Lett.* **34**, 3199 (2009).
- [14] L. Zhang, T. N. Dey, and J. Evers, *Phys. Rev. A* **87**, 043842 (2013).
- [15] A. G. Truscott, M. E. J. Friese, N. R. Heckenberg, and H. Rubinsztein-Dunlop, *Phys. Rev. Lett.* **82**, 1438 (1999).
- [16] N. Cui, Z. Gan, and L. Zhang, *Scientific Reports* **7** (2017), 10.1038/s41598-017-14456-z.
- [17] H. Shpaisman, A. D. Wilson-Gordon, and H. Friedmann, *Phys. Rev. A* **71**, 043812 (2005).
- [18] O. Firstenberg, P. London, M. Shuker, A. Ron, and N. Davidson, *Nature Physics* **5** (2009), 10.1038/nphys1358.
- [19] P. K. Vudyasetu, D. J. Starling, and J. C. Howell, *Phys. Rev. Lett.* **102**, 123602 (2009).
- [20] O. Firstenberg, M. Shuker, N. Davidson, and A. Ron, *Phys. Rev. Lett.* **102**, 043601 (2009).
- [21] S. Sharma and T. N. Dey, *Phys. Rev. A* **96**, 053813 (2017).
- [22] J. A. Andersen, M. E. J. Friese, A. G. Truscott, Z. Ficek, P. D. Drummond, N. R. Heckenberg, and H. Rubinsztein-Dunlop, *Phys. Rev. A* **63**, 023820 (2001).
- [23] D.-S. Ding, Z.-Y. Zhou, B.-S. Shi, X.-B. Zou, and G.-C. Guo, *Optics Communications* **285**, 1954 (2012).
- [24] S. R. Chanu and V. Natarajan, *Optics Communications* **295**, 150 (2013).
- [25] Z. Wang and J. Yin, *J. Opt. Soc. Am. B* **25**, 1051 (2008).
- [26] T. F. Gallagher, *Rydberg Atoms* (Cambridge University Press, 1994).
- [27] J. A. Sedlacek, A. Schwettmann, H. Kubler, R. Low, T. Pfau, and J. P. Shaffer, *Nature Physics* **8** (2012), 10.1038/nphys2423.
- [28] T. Vogt, C. Gross, T. F. Gallagher, and W. Li, *Opt. Lett.* **43**, 1822 (2018).
- [29] H. M. Kwak, T. Jeong, Y.-S. Lee, and H. S. Moon, *Optics Communications* **380**, 168 (2016).
- [30] N. S. Mallick, T. N. Dey, and K. Pandey, *Journal of Physics B* **50**, 195502 (2017).
- [31] X. Chu, Q. Sun, J. Wang, P. Lu, W. Xie, and X. Xu, *Scientific Reports* **5**, 18665 (2015).
- [32] R. L. Nowack, *Studia Geophysica et Geodaetica* **56**, 355 (2012).
- [33] S. Fu, T. Wang, Z. Zhang, Y. Zhai, and C. Gao, *Opt. Express* **25**, 20098 (2017).
- [34] P. Li, Y. Zhang, S. Liu, H. Cheng, L. Han, D. Wu, and J. Zhao, *Opt. Express* **25**, 5821 (2017).
- [35] F. Gori, G. Guattari, and C. Padovani, *Optics Communications* **64**, 491 (1987).
- [36] J. Han, T. Vogt, and W. Li, *Phys. Rev. A* **94**, 043806 (2016).
- [37] T. Vogt, C. Gross, J. Han, S. B. Pal, M. Lam, M. Kiffner, and W. Li, *Phys. Rev. A* **99**, 023832 (2019).
- [38] L. Zhang and J. Evers, *Phys. Rev. A* **89**, 013817 (2014).
- [39] O. Firstenberg, M. Shuker, A. Ben-Kish, D. R. Fredkin, N. Davidson, and A. Ron, *Phys. Rev. A* **76**, 013818 (2007).
- [40] O. Firstenberg, M. Shuker, R. Pugatch, D. R. Fredkin, N. Davidson, and A. Ron, *Phys. Rev. A* **77**, 043830 (2008).
- [41] P. R. Berman, J. E. M. Haverkort, and J. P. Woerdman, *Phys. Rev. A* **34**, 4647 (1986).
- [42] S. Singh and G. S. Agarwal, *J. Opt. Soc. Am. B* **5**, 2515 (1988).
- [43] I. Novikova, A. B. Matsko, and G. R. Welch, *J. Opt. Soc. Am. B* **22**, 44 (2005).
- [44] M. A. Kumar and S. Singh, *Phys. Rev. A* **79**, 063821 (2009).
- [45] R. Chrapkiewicz, W. Wasilewski, and C. Radzewicz, *Optics Communications* **317**, 1 (2014).
- [46] R. M. Jenkins, E. E. Mikhailov, and I. Novikova, *J. Opt. Soc. Am. B* **36**, 890 (2019).
- [47] S. Sharma and T. N. Dey, *J. Opt. Soc. Am. B* **36**, 960 (2019).
- [48] G. S. Agarwal, *Quantum Optics* (Cambridge University Press, 2012).
- [49] H. R. Hamed, M. Sahrai, H. Khoshshima, and G. Juzeliūnas, *J. Opt. Soc. Am. B* **34**, 1923 (2017).
- [50] K. Islam, A. Bandyopadhyay, B. C. Das, S. Saha, S. De, and D. Bhattacharyya, *J. Opt. Soc. Am. B* **34**, 2550 (2017).
- [51] G. P. Agrawal and D. N. Pattanayak, *J. Opt. Soc. Am.* **69**, 575 (1979).
- [52] Y. Zhou, J. Zhao, Z. Shi, S. M. H. Rafsanjani, M. Mirhosseini, Z. Zhu, A. E. Willner, and R. W. Boyd, *Opt. Lett.* **43**, 5263 (2018).